RESEARCH ARTICLE | SEPTEMBER 15 2023

Sub-quarter micrometer periodically poled Al₀,₅, Sc₀,₃₂N for ultra-wideband photonics and acoustic devices ⊘

Zichen Tang (1); Giovanni Esteves (1); Roy H. Olsson, III 2 (1)



J. Appl. Phys. 134, 114101 (2023) https://doi.org/10.1063/5.0161423





CrossMark

500 kHz or 8.5 GHz? And all the ranges in between.

Lock-in Amplifiers for your periodic signal measurement









Sub-quarter micrometer periodically poled Al_{0.68}Sc_{0.32}N for ultra-wideband photonics and acoustic devices

Cite as: J. Appl. Phys. 134, 114101 (2023); doi: 10.1063/5.0161423 Submitted: 9 June 2023 · Accepted: 27 August 2023 · Published Online: 15 September 2023







Zichen Tang, 1 D Giovanni Esteves, 2 D and Roy H. Olsson, III D



AFFILIATIONS

- ¹Electrical and Systems Engineering Department, University of Pennsylvania, Philadelphia, Pennsylvania 19104, USA
- ²Microsystems Engineering, Science and Applications (MESA), Sandia National Laboratories, Albuquerque, New Mexico 87123, USA

ABSTRACT

In this study, we demonstrate the ability of polarity inversion of sputtered aluminum scandium nitride thin films through post-fabrication In this study, we demonstrate the ability of polarity in the processes with domain widths as small as 220 nm at a periodicity of 440 nm. An approach using photo- and electron-beam integraphy of generate sub-quarter micrometer feature size with adjustable duty cycle through a lift-off process is presented. The film with a coercive field E_c^+ of 5.35 MV/cm was exercised first with a 1 kHz triangular double bipolar wave and ultimately poled with a 0.5 kHz double monopolar E_c^+ of 5.35 MV/cm was exercised first with a 1 kHz triangular double bipolar wave and ultimately poled with a 0.5 kHz double monopolar E_c^+ of 5.35 MV/cm was exercised first with a 1 kHz triangular double bipolar wave and ultimately poled with a 0.5 kHz double monopolar E_c^+ of 5.35 MV/cm was exercised first with a 1 kHz triangular double bipolar wave and ultimately poled with a 0.5 kHz double monopolar E_c^+ of 5.35 MV/cm was exercised first with a 1 kHz triangular double bipolar wave and ultimately poled with a 0.5 kHz double monopolar E_c^+ of 5.35 MV/cm was exercised first with a 1 kHz triangular double bipolar wave and ultimately poled with a 0.5 kHz double monopolar E_c^+ of 5.35 MV/cm was exercised first with a 1 kHz triangular double bipolar wave and ultimately poled with a 0.5 kHz double monopolar E_c^+ of 5.35 MV/cm was exercised first with a 1 kHz triangular double bipolar wave and ultimately poled with a 0.5 kHz double monopolar E_c^+ of 5.35 MV/cm was exercised first with a 1 kHz triangular double bipolar wave and ultimately poled with a 0.5 kHz double monopolar E_c^+ of 5.35 MV/cm was exercised first with a 1 kHz triangular double bipolar wave and ultimately poled with a 0.5 kHz double monopolar E_c^+ of 5.35 MV/cm was exercised first with a 1 kHz triangular double bipolar wave and ultimately poled with a 0.5 kHz double monopolar E_c^+ of 5.35 MV/cm was exercised first with a 1 kHz triangular double bipolar wave and ultimately poled with a 0.5 kHz double monopolar E_c^+ of 5.35 MV/cm was exercised fir acterized through potassium hydroxide wet etching as well as piezoresponse force microscopy (PFM). Well-distinguished boundaries between the oppositely polarized domain regions were confirmed through the phase diagram of the PFM results. The relationship between the electrode width, poling voltage, and domain growth was experimentally studied and statistically analyzed, where 7.96 nm/V domain & width broadening vs escalating poling voltage was observed. This method produces extremely high domain spatial resolution in III-nitride materials via poling and is transferable to a CMOS-compatible photolithography process. The spatial resolution of the periodically poled Al_{0.68}Sc_{0.32}N is suitable for second-harmonic generation of deep ultraviolet through quasi-phase-matching and RF MEMS operating in the X-Band spectrum.

Published under an exclusive license by AIP Publishing. https://doi.org/10.1063/5.0161423

I. INTRODUCTION

The synthesis of highly c-axis oriented aluminum scandium nitride (AlScN)¹ and the opportune revelation of its ferroelectricity² opened the door to many new applications. The photonic integrated circuit (PIC) is widely regarded as one of the most promising post-Moore era technologies. While extensive research has been conducted in silicon integrated photonics,3-5 the path to visible light and beyond remains less explored. Over the years, interest of PICs operating in the UV spectrum has been growing as it holds promise for spectroscopic studies, 6-8 optical atomic clocks, 9,10 electro-opto mechanics, 11 signal processing, 12 fluorescence microscopy, 13,14 and quantum computing. 15-18 Wurtzite III-nitride semiconductors have direct bandgaps, 19 with aluminum nitride (AlN) exhibiting the largest bandgap ($E_g = 6.2 \text{ eV}$) of them all, allowing the propagation and generation^{20–27} of light to the deep ultraviolet (DUV) spectrum.

However, with all the progress that has been $made^{26,28-32}$ in the LED industry, challenges in DUV light generation are still prevalent such as high defect density,³³ deficient current injection efficiencies,³⁴ and polarization field-induced charge separation.³⁵ These challenges result in an order of magnitude drop in the external quantum efficiencies (EQEs) compared to their longer wavelength (>365 nm) counterparts.2

Second-harmonic generation (SHG) is an alternative approach 36,37 to tackle these challenges by exploiting optical nonlinearity of a medium, which has been demonstrated in AlN via a variety of methods³⁸⁻⁴⁰ with wavelengths down to 306 nm.⁴⁰ The largest second-order nonlinear coefficient $\chi^{(2)}$ in AlN is dictated by the $\chi^{(2)}$ d_{33} coefficient, and it is measured to be 5.1 ± 0.4 pm/V (at 1550 nm) for sputtered⁴¹ AlN. This number is considerably lower than that (25.2 pm/V at 1064 nm) of LiNbO₃, one of the most commonly used on-chip nonlinear optical materials. 42,43 However,

a) Author to whom correspondence should be addressed: rolsson@seas.upenn.edu

Yoshioka *et al.* have measured the $\chi^{(2)}$ of sputtered Al_{1-x}Sc_xN with Sc alloying up to 36% and found that the d_{33} increases to 62.3 ± 5.6 pm/V, which is a 12× increase compared to AlN and 2× higher than LiNbO₃. On the other hand, for a given pump field A_1 , the excited SHG field A_2 into the depth L of the nonlinear medium can be written as⁴⁴

$$|A_2(L)|^2 = \frac{4\omega^2}{n_{2\omega}^2 c^2} \left[\chi^{(2)}\right]^2 |A_1|^4 L^2 \operatorname{sinc}^2\left(\frac{\Delta kL}{2}\right),\tag{1}$$

with Δk being the phase mismatch for forward transmission and is denoted by

$$\Delta k = 2k_1 - k_2 = 2\frac{n_\omega \cdot \omega}{c} - \frac{n_{2\omega} \cdot 2\omega}{c} = 2\frac{\omega}{c}(n_\omega - n_{2\omega}). \quad (2)$$

In the case of $\Delta k \neq 0$, the SHG wave will experience periodic SH generation and demolition. Thus, it is critically important for phase matching to be established to allow efficient SHG. There are two primary methods to achieve phase matching: birefringent phase matching (BPM) and quasi-phase matching (QPM). AlScN is a uniaxial crystal⁴⁵ where BPM usually applies, yet the difference between its ordinary refractive index n_0 and extraordinary refractive index n_e is not sufficiently high to allow BPM. QPM compensates the phase mismatch using the periodic inversion of the domain polarity P_s of the nonlinear crystal.⁴⁶ It yields the highest SHG efficiency through the utilization of much larger $\chi^{(2)}$ along other crystal axes excluded by the BPM and is the preferred method for SHG processes. The optical propagation loss of sputtered AlScN films at 1550 nm has been previously measured as 8.2 dB/cm for $Al_{0.80}Sc_{0.20}N$ and 17.2 dB/cm for $Al_{0.64}Sc_{0.36}N$, respectively, ⁴¹ when deposited using nearly identical sputtering conditions on sapphire substrates. Although sputtered films are often polycrystalline instead of a single-crystal, it does not necessarily suggest that these films carry higher optical losses when compared to films deposited by metal-organic chemical vapor deposition (MOCVD) or molecular beam epitaxy (MBE). For example, measurements of polycrystalline AlN films have demonstrated losses of 0.42 dB/cm, 47 similar to those achieved in epitaxial AlN films.⁴⁸ Moreover, it has been shown that by improving growth conditions, the measured bandgap of sputtered AlScN can approach the values derived from theoretical calculations. 49-51 Therefore, we conclude that high quality polycrystalline AlScN films are promising for nonlinear photonics.

Besides second-harmonic generation, another realm where periodically poled structures are useful is acoustics. Acoustic resonators with resonances of $10-1000 \, \text{MHz}$ have been studied via periodically poled LiNbO₃ (PPLN) and LiTaO₃ (PPLT) superlattices, ^{52–56} and most recently, a dual-mode resonator using reconfigurable periodic poling was realized in the periodically poled Al_{0.68}Sc_{0.32}N (PPASN) with frequencies up to 3 GHz and electro-mechanical coupling, $k_{\rm t}^2$, as high as 4.95%. ^{57,58} Scaling of PPASN to the dimensions required for PICs will also enable PP acoustic devices operating in the X-band (8–12 GHz), allowing the monolithic integration of multi-frequency filters on the same die.

The first PPLN devices were realized via temperature fluctuation during the Czochralski method of crystal growth⁵⁹ with coherence length $l_c = 3.4 \,\mu\text{m}$, almost two decades after the concept of QPM was initially proposed.^{60,61} Periodically poled thin film gallium nitride (GaN) periodicity of 250 nm⁶² was reported through Mg over-doping along with other methods, 63-67 quency conversion was observed. 64,67 In addition to these, periodically poled AlN with a domain size down to 600 nm has recently been achieved,⁶⁸ utilizing an annealed AlN buffer layer deposited at low temperature (650 °C), and SHG of 344 nm UV light was demonstrated.⁶⁹ While the above methods were able to intrinsically generate a periodically poled structure during film growth, they often involve high temperature procedures that make the process non-compatible with back-end CMOS processes. Alternatively, the polarity of the domains can be switched post-film deposition via E-beam charge injection,⁷⁰ laser poling,⁷¹ focused ion beam (FIB) Ga⁺ doping,⁷² or piezoresponse force microscopy (PFM) poling. These processes do avoid the use of high-temperature steps but are maskless fabrication steps and would face potential issues of scalability and cost for production. This paper reports periodic poling exploiting the ferroelectric properties of AlScN, where the polarity can be flipped with an applied electric field higher than the material coercive field E_c^+ . This method has been proven on a wide range of nonlinear crystals⁷⁴⁻⁷⁷ and is CMOS-compatible, rapid, and reversible.

In all the scenarios mentioned above, one vital criterion governing the device performance is the periodicity Λ of the periodically poled structure. In QPM, Λ for the first-order SHG is given by

$$\Lambda = 2l_c = \frac{2\pi c}{\omega_2 n_{2\omega} - \omega_1 n_{\omega}} = \frac{\lambda_{\omega}}{2(n_{2\omega} - n_{\omega})}.$$
 (3)

Hypothetically, for generating 266 nm light with 532 nm input $\stackrel{\text{\toparticle{2}}}{\text{light}}$ using periodically poled $\text{Al}_{0.68}\text{Sc}_{0.32}\text{N}$ through SHG, by extracting the dispersion curve reported by Baeumler *et al.*, taking $n_{532\text{nm}} = 2.261$ and $n_{266\text{nm}} = 2.861$, it can be calculated that $\Lambda = 443$ nm. For the PPASN acoustic device, assuming the sound velocity stays constant with scaling, based on the measurement reported by Rassay *et al.*, 57,58 for a device working at the X-band, yields $\Lambda = 600$ nm. These high-end applications require the formation of periodically poled domain sizes on the order of 200 nm, which is the subject of this paper.

II. EXPERIMENTAL METHODS

A. Fabrication of the periodically poled AIScN structure

1. Bottom electrode, AIScN film, and electrical contact

The fabrication process starts from an 8-in. high-resistivity Si wafer. A Ti/TiN/AlCu (0.5 wt. % Cu in Al) layer with a thickness of 20 nm/25 nm/50 nm was consecutively deposited on the wafer via sputtering. This electrode deposition process has been previously reported, and the highly orientated film stack (rocking curve FWHM \sim 1.3°, surface roughness $R_{\rm a} \sim 1.31$ nm) demonstrated strong suppression of secondary grains during AlScN film growth. After bottom electrode deposition, the wafer was then cleaved into 74×74 mm² dies for easier handling. Approximately 200 nm of

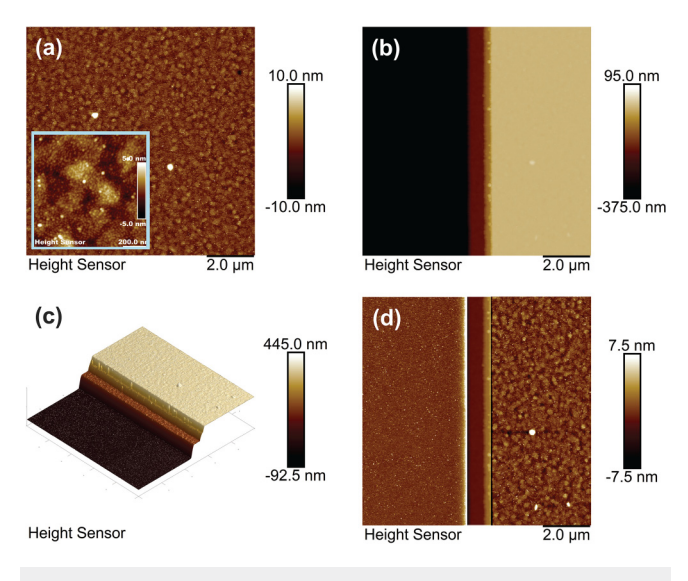


FIG. 1. AFM of the $Al_{0.68}Sc_{0.32}N$ film (a) on the AlCu bottom electrode, (b) at the boundary between the bottom electrode and the field Si substrate, (c) 3D reconstruction of the step height at the boundary, and (d) elevation of both the field region and the AlCu bottom electrode leveled for optimized contrast.

SiO₂ was deposited onto the substrate using an Oxford Plasma Lab 100 PECVD. The bottom electrode was patterned using a Heidelberg DWL 66+ laser writer and transferred to the SiO₂ hardmask through dry etching in an Oxford 80 plus Reactive-ion Etching (RIE) etcher by CHF₃/O₂ chemistry. The etching of the AlCu layer was carried out in the Transene Al Etchant Type A. After PR stripping, a homemade ammonia peroxide mixture (APM) solution was prepared following the recipe provided by Liu *et al.*⁷⁹ by mixing and heating NH₄OH:H₂O₂:H₂O = 1:2:5 at 60 °C, in which the remaining Ti/TiN layer was removed with a 2-min submersion. The sample was moved to the Denton Explorer14 Magnetron Sputter where it was sputter-etched for 30 min with Ar plasma. This step aims to annihilate the surface oxide on the AlCu bottom electrode and provide a highly oriented template for the proceeding AlScN growth.

The deposition of Al_{0.68}Sc_{0.32}N was conducted in an Evatec CLUSTERLINE® 200 II Physical Vapor Deposition System by co-sputtering from two 100 mm targets of Al (99.999%) and Sc (99.99%) in a pure nitrogen environment. The process conditions were described in a previous paper⁸⁰ with the exception of the omission of the gradient seed layer, which could add complexity to the poling process. In the end, 200 nm of nitrogen polar Al_{0.68}Sc_{0.32}N was deposited including a 15 nm AlN seed, which assisted in achieving high c-axis orientation while minimizing its role during poling. The images shown in Fig. 1 exhibit the surface condition of the Al_{0.68}Sc_{0.32}N film both on AlCu and at the boundary between the bottom electrode and the field areas.

The surface roughness on AlCu was measured to be $R_a = 1.09$ nm when sampled in the center of the bottom electrode, while it was $R_a = 1.10$ nm near the boundary. The inset in Fig. 1(a) shows well-developed AlScN grains inherited from the hexagonal

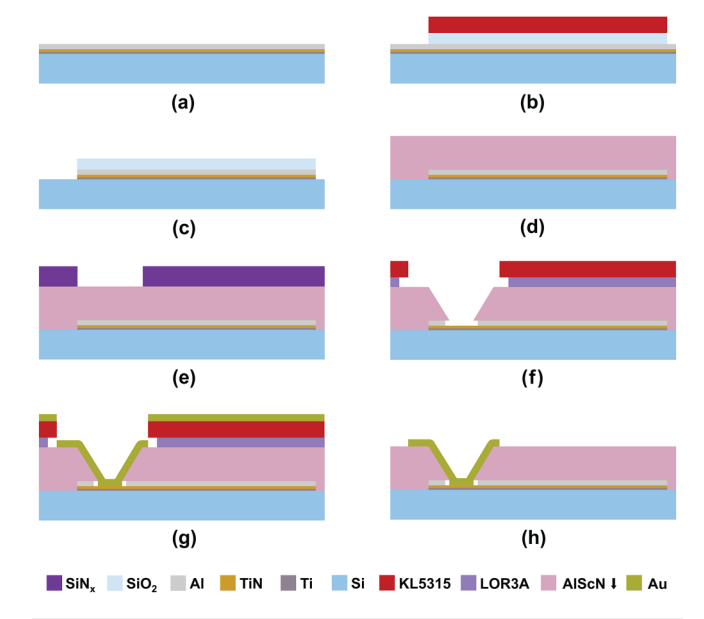


FIG. 2. (a) Deposition of Ti/TiN/AlCu on a high-resistivity silicon substrate; (b) deposition of PECVD SiO_2 and subsequent dry etching using KL5315 photoresist as a mask; (c) wet etching of AlCu, removal of KL5315, and wet etching of Ti/TiN; (d) stripping of SiO_2 , sputtering etch of the Al surface, and AlScN deposition, (e) PECVD SiN_x deposition, patterning, and the following photoresist removal; (f) KOH wet etching of AlScN, subsequent SiN_x stripping, and the patterning of KL5135-LOR3A double layer lift-off resist; (g) Ti/Au evaporation; and (h) lifting off evaporated Ti/Au. Film thickness and width are not drawn to scale.

close pack symmetry of the $\{111\}$ textured AlCu film. The profile from Fig. 1(b) shows a low occurrence of abnormally oriented grains (AOGs) where film growth quality was previously thought to be highly compromised due to the discontinuity at the substrate boundary. 81

To access the bottom electrode, a via was fabricated by wet etching of AlScN using 30 wt. % aqueous potassium hydroxide (KOH) at 45 °C with a $\rm SiN_x$ hardmask. A thorough study of this process was previously reported, ⁸⁰ and the etch stops at the TiN surface with around 2.5 μ m lateral etch of the AlCu beneath the AlScN film. The hardmask was removed using a CHF₃/O₂ dry etch in an Oxford 80 plus RIE. A double layer lift-off resist was spin-coated and patterned by direct writing. The sample was loaded into a Lesker PVD75 E-beam Evaporator and around 10 nm Ti/200 nm Au was deposited on the die. The film was finally lifted off with sonication and rinsed with de-ionized (DI) water, followed by an N₂ blow dry. The fabrication process to this step is summarized in Fig. 2.

2. Periodic poling gratings

To achieve the 220 nm periodically poled domain size, e-beam lithography (EBL) was employed. It should be noted that EBL was used solely for the purpose of resolution, and the processes would be high volume manufacturable through the use of a DUV stepper such as those commonly employed at the 180 nm process node. The sample was further cleaved into smaller dies of $37 \times 37 \text{ mm}^2$,

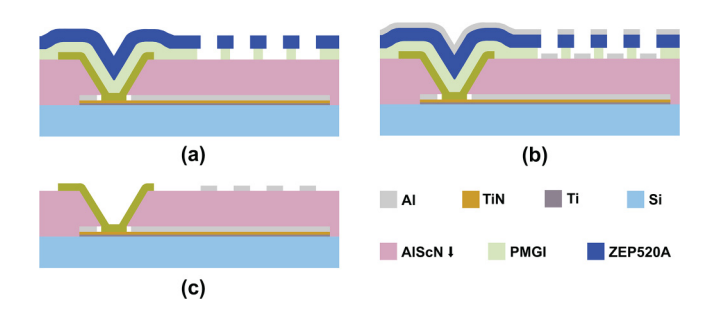


FIG. 3. (a) Spin coating and EBL patterning of ZEP-PMGI bi-layer resists; (b) e-beam evaporation of the poling electrode onto the lift-off layer; and (c) the poling electrode lifted-off.

and a ZEP520A-PMGI bi-layer lift-off resist was spun on to generate the desired undercut for a clean lift-off. The sample was exposed in an Elionix ELS-7500EX E-Beam Lithography System with 50 kV accelerating voltage, 100 pA current, and 125 μC/cm² regular doses. Afterward, the ZEP520A and PMGI were sequentially developed, followed by DI water rinse and N2 blow dry. The sample was descummed in a Jupiter II RIE Plasma Etcher with O₂ plasma and transferred into a Lesker PVD75 E-beam Evaporator. Approximately 10 nm Ti/150 nm Al was e-beam evaporated onto the film and lifted off. Figure 3 illustrates the EBL process in which the periodic poling gratings were formed.

During the process development, numerous samples were fabricated where their poling electrodes were elongated such that cross section scanning electron microscopy (SEM) could be performed to assess the electrodes before ferroelectric switching. Figure 4 gives an example of the cross section image of the poling gratings after

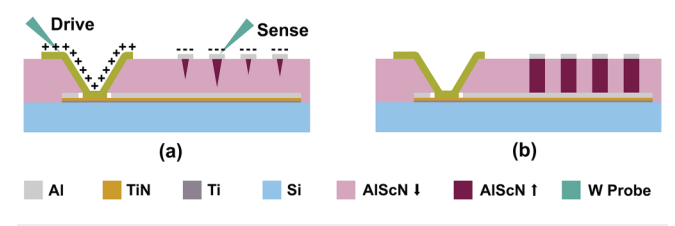


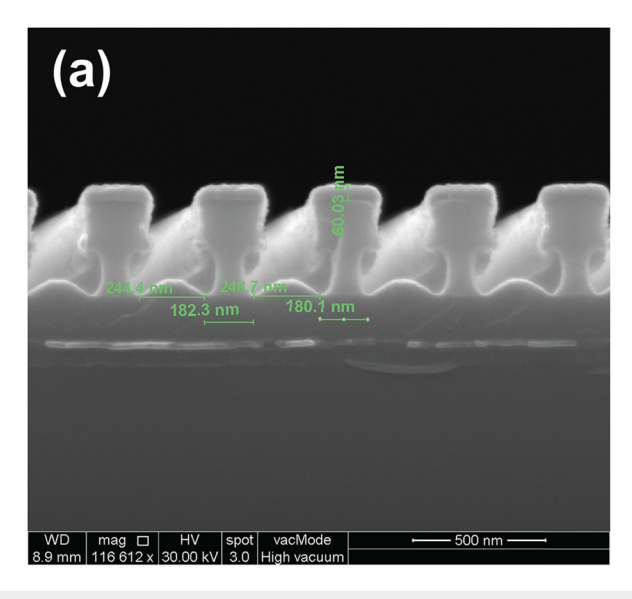
FIG. 5. (a) Probe step and domain growth during the switching of AIScN; and (b) the state of the film when poling is completed. Note that the gratings were connected by a bus out of the plane in the physical layout.

10 nm/50 nm of Ti/Al was deposited during a test run and a top-down view of a sample with 10 nm/150 nm of Ti/Al lifted-off (in both cases, the periodicity of $\Lambda = 440$ nm was maintained).

B. Ferroelectric switching

The ferroelectric switching behavior of AlScN has been extensively studied82-86 following the discovery of its ferroelectricity.2 Although a number of methods can be applied for the poling setup, we choose to adapt the top-sense/bottom-drive method for its simplicity and high success rate. In this configuration, the voltage is supplied to the bottom electrode through a tungsten probe, and the charge was returned and measured from the top-electrode. The poling procedure is illustrated in Fig. 5.

Poling was performed with a Radiant Precision Premier II tester. A series of triangular double bipolar waves at 1 kHz fre- of quency were used first to exercise the sample so as to reduce the mimprint" effect in the film. The amplitude of the waves gradually increases from 40 to 100 V with a 10 V increment between each run, followed by an increment of 1 V until the electric field



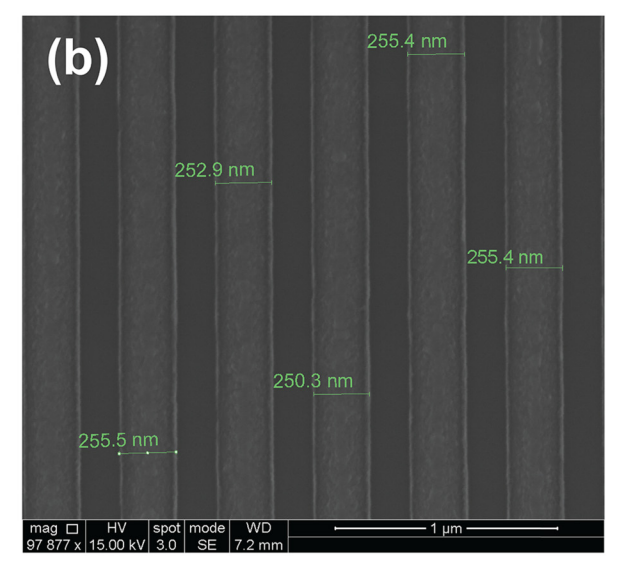


FIG. 4. (a) Cross section SEM of the poling grating after 10 nm of Ti and 50 nm of Al was evaporated in a test run; and (b) the device surface after 10 nm/150 nm Ti/Al was evaporated and lifted off through removal of the resist.



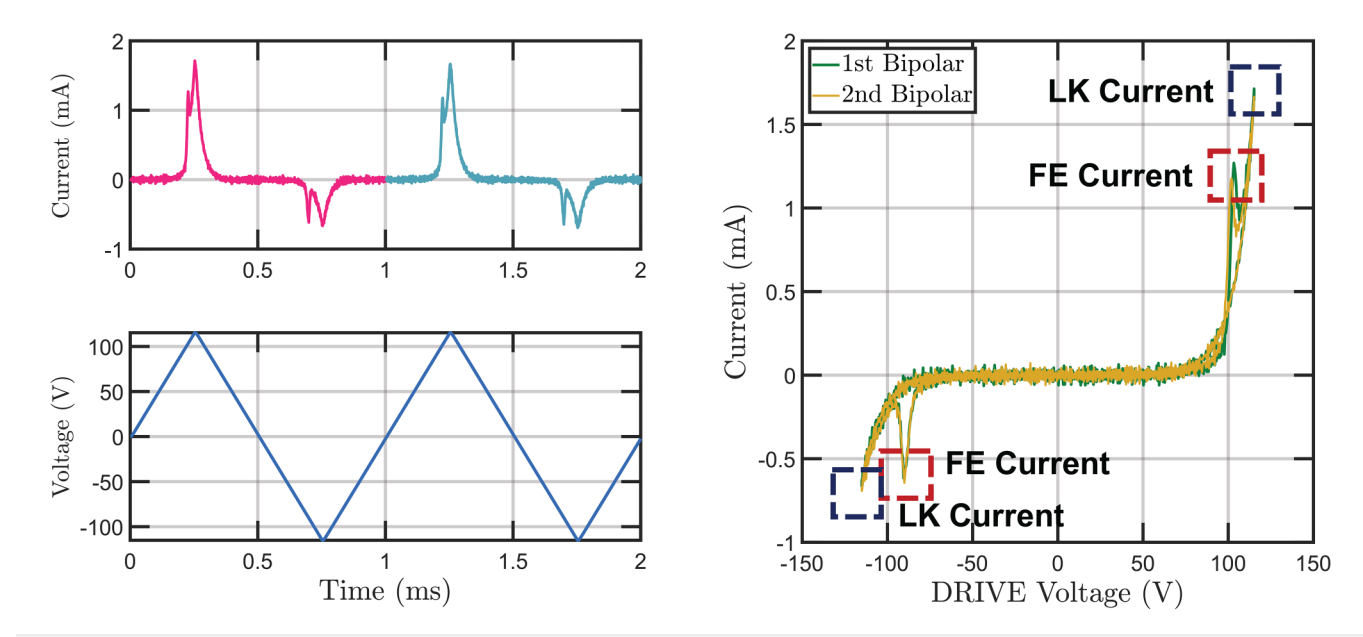


FIG. 6. (a) I-t (b) V-t, and (c) I-V plot during the exercising of the film with a double bipolar triangular wave with the poling voltage of 117 V. The coercive voltage V^c decreased from 103.3 V in the first bipolar cycle (shown in green) to 101.9 V in the succeeding cycle (shown in yellow).

exceeds the coercive field E_c^+ (5.35 MV/cm determined with hysteresis loop) and reaches the poling field, E_p . Finally, a triangular double monopolar wave of positive up with a 0.5 kHz frequency was applied to fix the poling state in the metal polar (M-polar) condition. The current vs time (I-t) and current vs voltage (I-V) plots exhibit separate and distinguishable peaks originating from ferroelectric (FE) and leakage (LK) currents. The remnant polarization was calculated to be $108.5 \mu \text{C/cm}^2$ with results from a thicker film, which fits the measurement given by Fichtner et al.2 (Fig. 6).

III. RESULTS AND ANALYSIS

A. Polarity verification using KOH wet etching

On the test sample, the periodic poling gratings were divided into eight sub-arrays. Each sub-array was made of 100 poling gratings connected by a bus such that it could be poled individually. For demonstration purposes, arrays 2 and 7 were not poled, while the rest of the arrays were poled with the aforementioned process with $V_p = 120 \text{ V}$. Following the poling, the electrodes were stripped by sequential submerging in Al Etchant Type A and APM solution. The effect of poling can be seen immediately in Figs. 7(a) and 7(b) where the regions of the samples that were poled (metal-polar or M-polar) show a different color compared to the non-poled regions (nitrogen-polar or N-polar).

To further characterize the switching effect, the sample was submerged in 30 wt. % KOH solution at 45 °C for 2 min, a time long enough to remove 3× the thickness of the N-polar Al_{0.68}Sc_{0.32}N.⁸⁰ As a result, the N-polar region was completely eliminated, while the M-polar region remained after extensive

etching as shown in Fig. 7(c). The etching behavior of N-polar and M-polar films in hot KOH matches the descriptions given by previous researchers^{2,87,88} and provides strong evidence of successful ferroelectric switching. Figure 7(c) presents a variety of rainbow-tone patterns on the M-polar grating region that do not arise from the M-polar AlScN etching in KOH but rather are from an optical effect (Newton's rings) caused by the local under etching of the Al bottom electrode and the Si substrate from the pre-penetration $\frac{\sigma}{2}$ of defects in the film (most likely, over the N-polar region). Figure 7(d) was able to demonstrate via tilted SEM images that the M-polar film survives the KOH etching without thickness reduction, even with the bending of the film that is due to the loss of the Al bottom electrode from lateral etching in the KOH. Figure 7(e) was taken from the center of a poled grating. From the figure, M-polar AlScN formed under the metalized gratings was unetched while the N-polar regions were removed. The gap between the M-polar regions is measured to be 121.5 nm, which consists of two 47.7 nm sidewall regions of the surviving M-polar film and one 26 nm wide pure void down to the substrate. With trigonometry, the sidewall of the III-polar grating is calculated to be 76°, which is considerably larger than its N-polar counterpart. 80 The same phenomenon was also observed at the boundary of the poled and nonpoled arrays in Fig. 7(f), with the exception of a smaller sidewall profile. In all cases, the periodicity of the M-polar AlScN regions was maintained at 440 nm, and the width of M-polar gratings was kept at around 315 nm, indicating a duty cycle of around 71%.

B. KOH wet etching susceptibility to poling field E_p

While the M-polar region in this sample withstood KOH etching after being poled at 120 V, often it is desirable to pole the

broadening, and spontaneous back switching. To assess the domain polarity of the film after poling, piezoresponse force microscopy

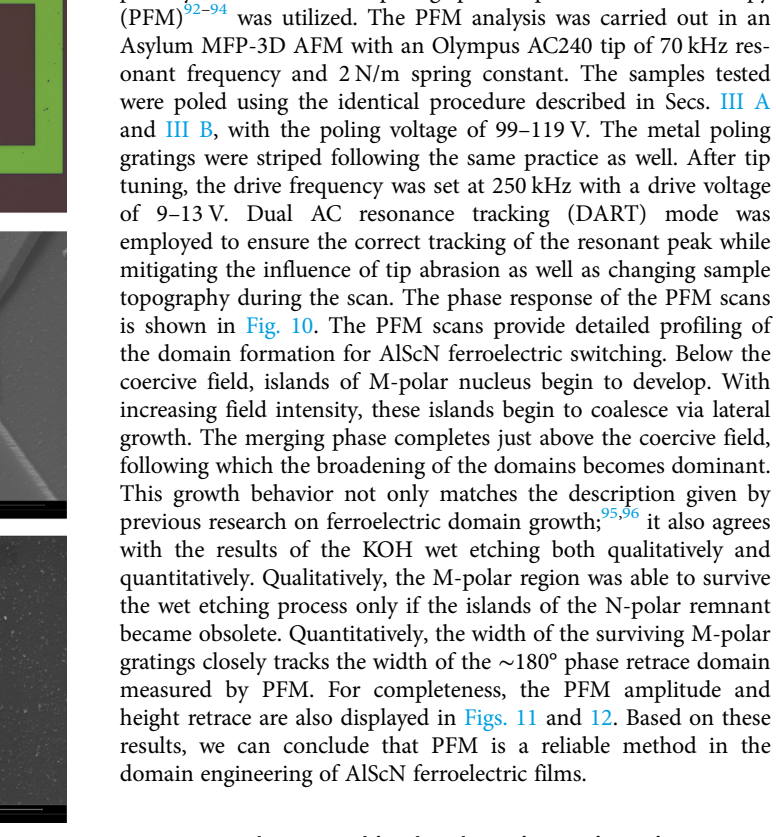


FIG. 7. (a) Optical image of a grating array after the poling of sub-gratings 1, 3, 4, 5, 6, and 8 at a poling voltage of 120 V; (b) the surface of the film after stripping of the poling electrodes in Al Etchant Type A and APM solution. The poled region exhibits an apparent lighter tone compared to regions that remained N-polar; (c) optical image of the sample after KOH wet etching, the non-poled regions (2, 7) were completely removed; (d) tilted SEM image of the boxed region; (e) SEM image of the film surface in the center of the poled sub-grating; and (f) the SEM image of the film surface at the boundary of poled sub-grating.

(d)

sample at a lower voltage to stay well below the breakdown field $E_{\rm b}$. We have stated earlier that the coercive field, E_c^+ , was determined by hysteresis loop measurements or, more specifically, by identifying the ferroelectric current on the I-V plots in Fig. 8. To study the effect of the poling voltage on the PP structure, samples poled at different voltages were etched in KOH post-poling with subsequent SEM images shown in Fig. 9. The coercive field found using the KOH etching results is in strong agreement with that found utilizing the I-V plots in Fig. 8.

C. PFM evaluation of domain growth vs polarization field Ep

Domain growth is a sophisticated kinetic process with multiple phases involved, 74,89-91 including nucleation, forward growth,

Duty-cycle control is vital for the application cases of AlScN mentioned in Sec. I. Taking QPM, for example, the effect of random duty-cycle errors was studied thoroughly by Fejer et al., 97 in which the normalized SHG efficiency is calculated to be

$$\langle \hat{\eta} \rangle = e^{-\frac{\sigma_{\Phi}^2}{2}} + \frac{1}{N} \left(1 - e^{-\frac{\sigma_{\Phi}^2}{2}} \right), \tag{4}$$

where σ_Φ^2 is given by $\sigma_\Phi^2 = \pi^2 \sigma_l^2 / l_c^2$ and N is the number of the layers in the periodically poled structure. With N sufficiently large and only moderate errors considered, Eq. (4) reduces to

$$\langle \hat{\eta} \rangle \approx e^{-\frac{\sigma_0^2}{2}} \approx 1 - \frac{\pi^2 \sigma_l^2}{2l_c^2},$$
 (5)

with σ_l^2 being the variance of random duty-cycle errors and l_c being the coherence length. The threshold of 50% SHG can be maintained if the RMS value of the error satisfies $\sigma_1/l_c < 0.375$.

To adjust the duty cycle of the metalized region, a design of experiment was performed by adjusting the EBL dose and exposure linewidth in the design profile. By employing a strategy known as overdose, undersize (ODUS), a wide range of grating linewidths can

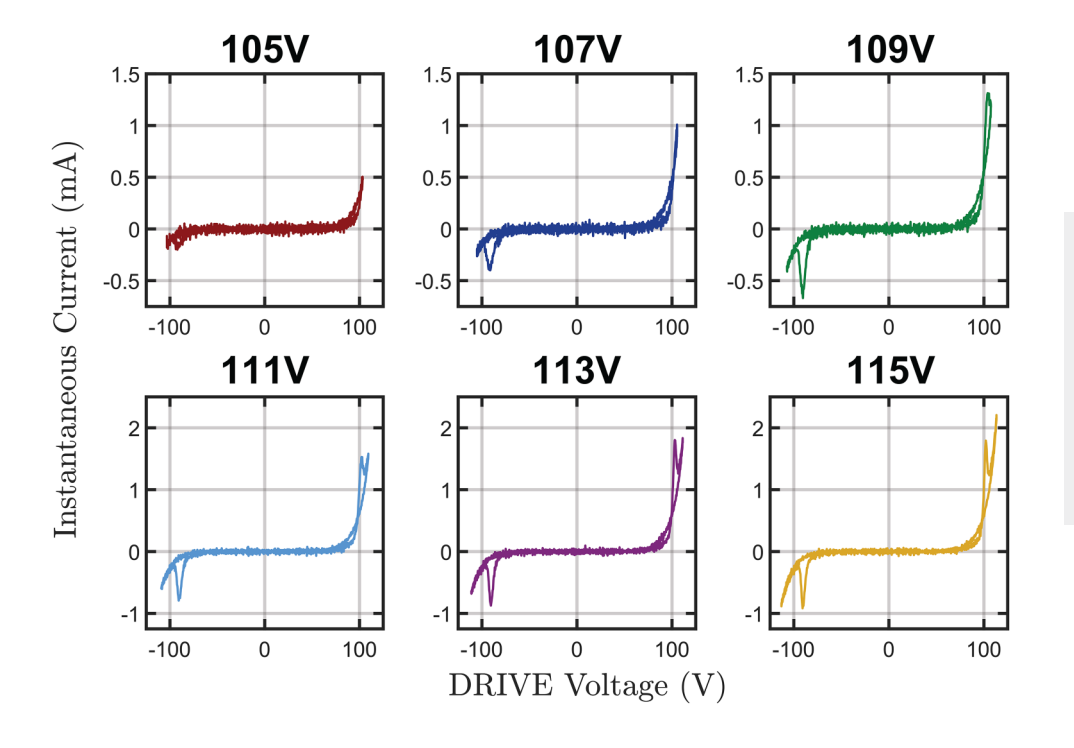


FIG. 8. The current vs the driving voltage plots, with the poling voltage ranging from 105 to 115 V with a 2 V step. When the poling voltage reaches 107 V, the ferroelectric induced current was notably distinguished from the total current for the first time during the film transition from the M-polar to the N-polar state, with its peak sitting at $-90 \text{ V}_{\odot}^{\star}$ Thus, we conclude the coercive field E_{\odot}^{\star} to be -90 V/200 nm = 5.35 MV/cm, while E_{\odot}^{\star} to be -90 V/200 nm = -4.50 MV/cm.

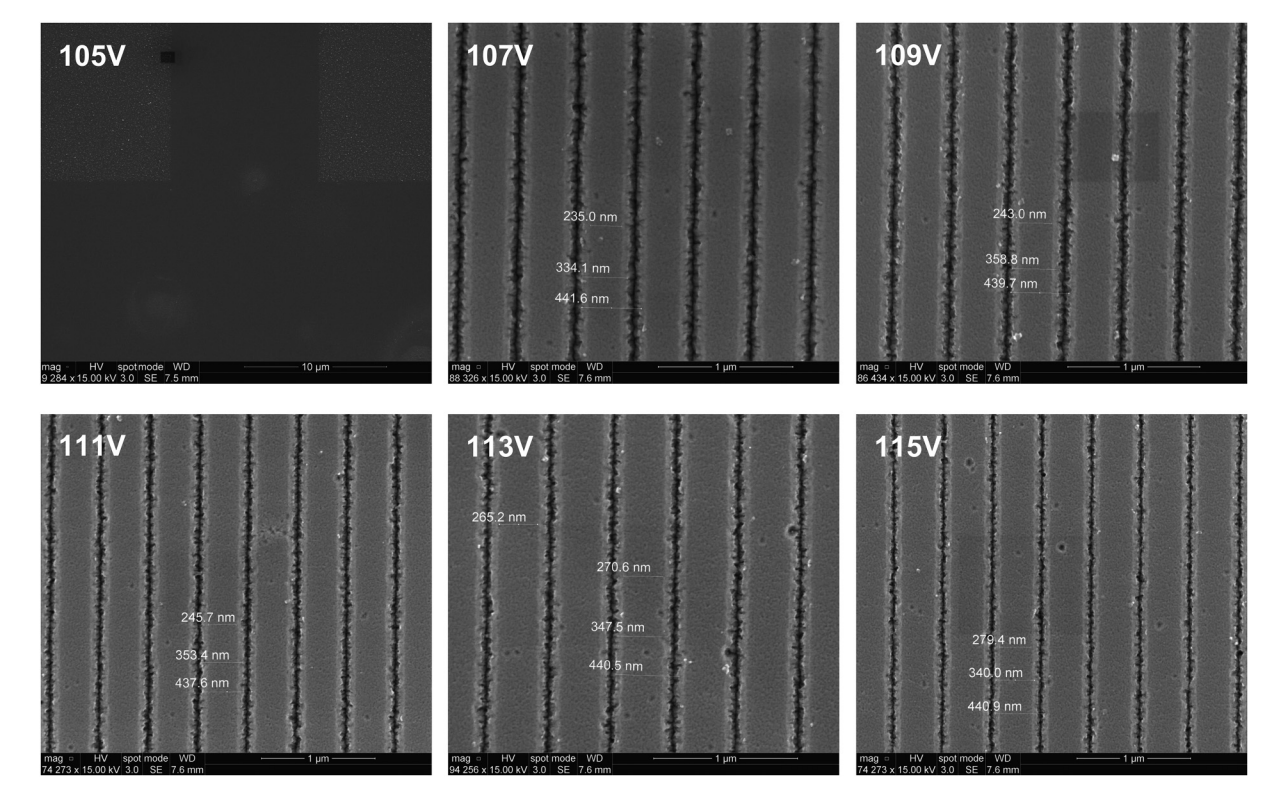


FIG. 9. SEM of the sample surface post-KOH wet etching after being poled at different voltages. The etching condition is the same as used before (30 wt. %, 45 °C, 2 min). The film poled at or above the coercive field remained after exposure to the KOH etchant.

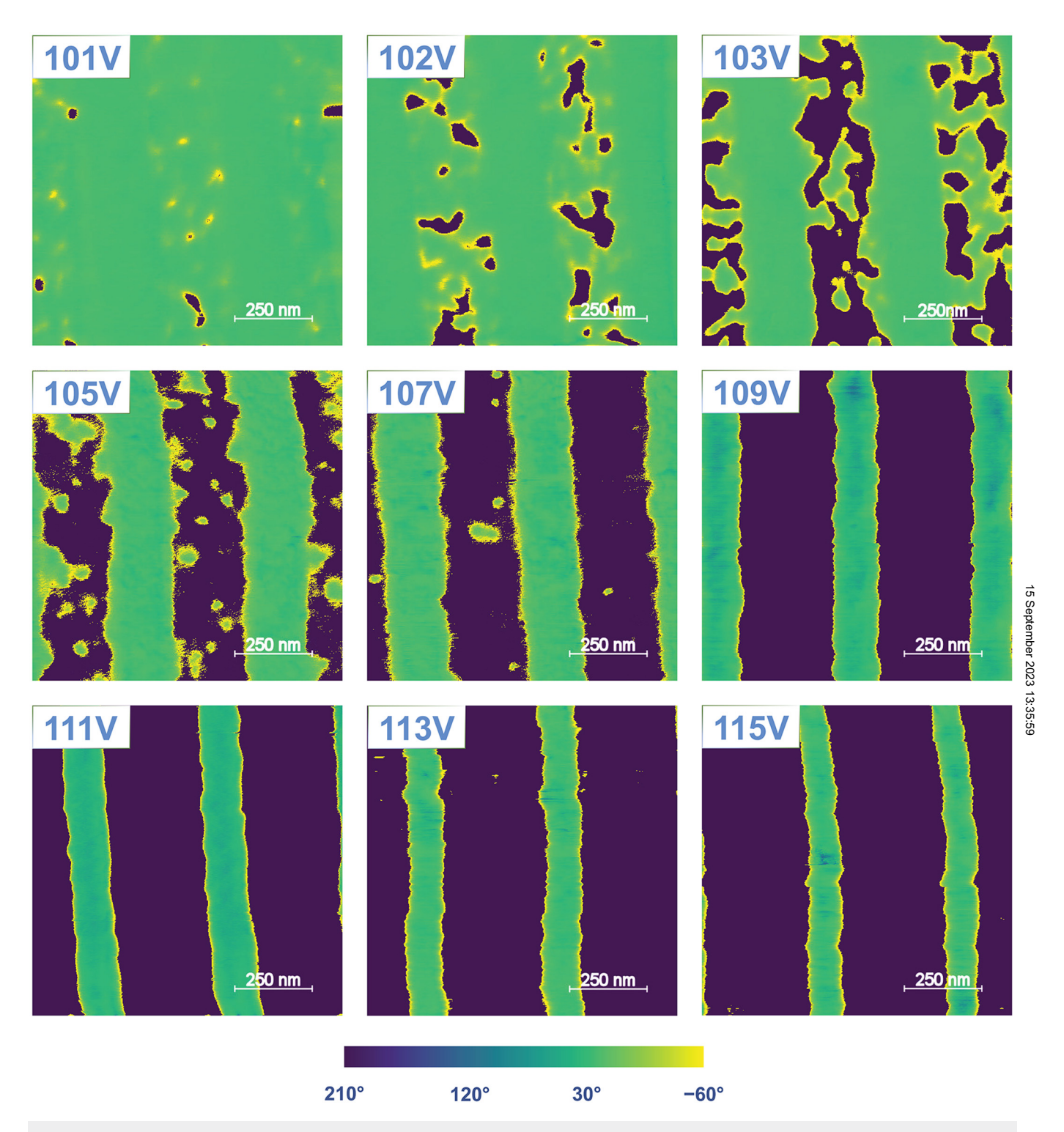


FIG. 10. PFM phase retrace results. The M-polar region is shown in dark blue, while the N-polar region is presented in light green, with the phase difference between the two at around 180°. Note that the curvature at the top/bottom of certain images was due to the effect of the sample moving upon the engagement of the PFM tip in the absence of vacuum in Asylum's high voltage sample holder.

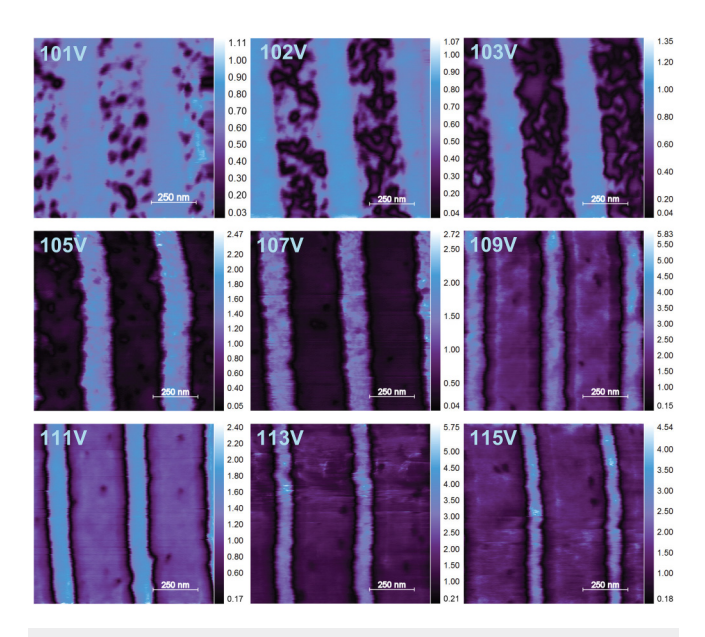


FIG. 11. PFM amplitude retrace results. These are the piezoelectric responses to the applied electrical field. Value bar of each graph has the unit of (nm) and was rendered to the (min, max) of each scan for full dynamic range exhibition. A general trend here is that the value increases with increasing poling voltage, as the M-polar regions are becoming more developed. It should be noted, however, that the sample with poling voltages of 105, 107, 109, 113, and 115 V were scanned with different integral gains and resonance Q.

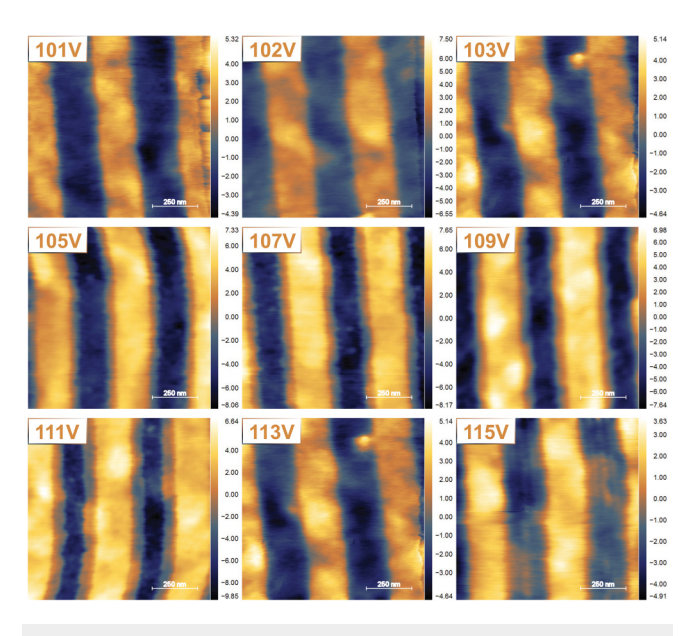


FIG. 12. PFM height retrace results. A step height of approximately 10 nm is observed in unpoled samples based on where the electrodes were located prior to removal using wet etching, as shown for the sample where 101 V was applied to the electrodes prior to their removal. When the poling voltage exceeds the coercive field, the step height between where the metal electrodes were located (now poled M-polar) and where they were not located increases to ~16 nm as shown for the scans where 105, 107, 109, and 111 V were applied to the poling electrodes prior to their removal.

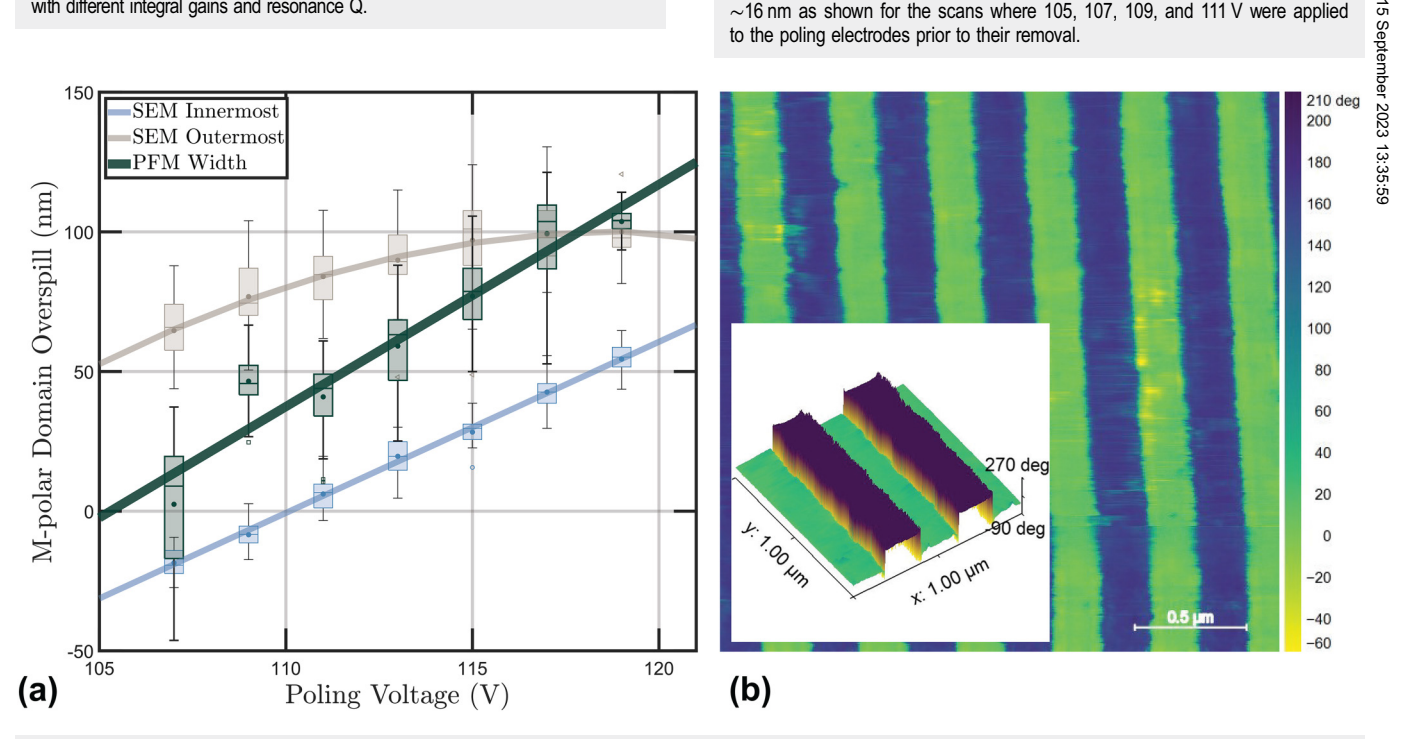


FIG. 13. (a) M-polar domain width exceeding the 258 nm poling electrodes based on SEM/PFM measurements with respect to the poling voltage. (b) The fabricated PPASN sample with 220 nm M-polar domain width and 440 nm periodicity by poling 202 nm wide electrodes at 113 V, and the inset demonstrated the 3D-presentation of the phase response inside a $1 \times 1 \mu m^2$ region.

be achieved while keeping the periodicity. The relationship between the domain side growth and poling voltage was measured separately for both the SEM on wet etched samples and the PFM phase retrace results. For SEM images, in particular, since KOH wet etching generated a corrugated sidewall by exposing the $\{10\overline{11}\}$ plane of the hexagonal close-packed (HCP) crystal structure of AlScN that extended all the way to the top planes, it was somewhat arbitrary to identify the precise width of the remaining M-polar domain. Therefore, both the innermost and outermost widths were measured. The former corresponds to the darker region appearing in the SEM image where we are absolutely certain it was within the M-polar domain, while the latter extends to the lighter region where it was sufficiently close to the sidewall. As shown in Fig. 13(a), when being poled with a mean poling electrode width of 258 nm, the over-spilled M-polar domain width measured directly from the PFM phase retrace result falls nicely between the innermost and outermost range characterized by KOH wet etching using SEM. By taking the linear regression of the average PFM domain width, an over-spilled M-polar width of 7.96 nm per 1 V increment of the poling voltage was observed. With this knowledge in mind, a 50% duty-cycle PPASN structure was fabricated experimentally reducing the poling electrode width from 258 to 202 nm and utilizing a 113 V poling voltage. The phase response of the sample is shown in Fig. 13(b).

IV. CONCLUSION

A systematic study of domain engineering in AlScN through ferroelectric switching is reported. A sample with a precision tailored 220 nm domain size and 50% duty cycle was achieved via periodic poling of sputtered 200 nm thick AlScN. A method combining photo- and e-beam lithography to generate sub-quarter-micrometer-width poling electrodes was presented and examined. The ferroelectric switching was performed by exercising the film first with 1 kHz double bipolar triangular waves, and polarization fixation was achieved via 0.5 kHz double monopolar triangular waves. The relationship between the poling voltage and domain formation was characterized by 30 wt. % KOH wet etching at 45 °C, and the coercive field, E_c^+ , of 5.35 MV/cm deduced from the ferroelectric current was verified. The domain growth vs polarization field was also studied via piezoresponse force microscopy and cross-matched with KOH etching results. Approximately 7.96 nm/V domain width overgrowth was observed. The methods presented in this research provide a high-fidelity approach for fabricating and characterizing PPASN, which will benefit the future formation of nonlinear optic and acoustic devices.

ACKNOWLEDGMENTS

This work was funded in part by the NSF Career Award (No. 1944248). This work was carried out in part at the Singh Center for Nanotechnology at the University of Pennsylvania, a member of the National Nanotechnology Coordinated Infrastructure (NNCI) network, which is supported by the National Science Foundation (NSF) (Grant No. HR0011-21-9-0004). Sandia National Laboratories is a multi-mission laboratory managed and operated by National Technology & Engineering Solutions of Sandia, LLC (NTESS), a wholly owned subsidiary of Honeywell International Inc., for the U.S. Department of Energy's National Nuclear Security

Administration (DOE/NNSA) under Contract No. DE-NA0003525. This written work is authored by an employee of NTESS. The employee, not NTESS, owns the right, title, and interest in and to the written work and is responsible for its contents. Any subjective views or opinions that might be expressed in the written work do not necessarily represent the views of the U.S. Government. The publisher acknowledges that the U.S. Government retains a non-exclusive, paid-up, irrevocable, world-wide license to publish or reproduce the published form of this written work or allow others to do so for U.S. Government purposes. The DOE will provide public access to results of federally sponsored research in accordance with the DOE Public Access Plan.

AUTHOR DECLARATIONS

Conflict of Interest

The authors have no conflicts to disclose.

Author Contributions

Zichen Tang: Conceptualization (equal); Data curation (equal); Formal analysis (equal); Investigation (equal); Methodology (equal); Software (equal); Validation (equal); Visualization (equal); Writing – original draft (equal). Giovanni Esteves: Conceptualization (equal); Data curation (supporting); Funding acquisition (supporting); Investigation (supporting); Methodology (supporting); Project administration (supporting); Visualization (supporting); Writing – review & editing (equal). Roy H. Olsson III: Conceptualization (equal); Data curation (equal); Formal analysis (equal); Funding acquisition (equal); Investigation (equal); Methodology (equal); Project administration (equal); Resources (equal); Supervision (equal); Writing – review & editing (equal).

DATA AVAILABILITY

The data that support the findings of this study are available from the corresponding author upon reasonable request.

REFERENCES

- ¹M. Akiyama, T. Kamohara, K. Kano, A. Teshigahara, Y. Takeuchi, and N. Kawahara, "Enhancement of piezoelectric response in scandium aluminum nitride alloy thin films prepared by dual reactive cosputtering," Adv. Mater. **21**(5), 593–596 (2009).
- ²S. Fichtner, N. Wolff, F. Lofink, L. Kienle, and B. Wagner, "AlScN: A III–V semiconductor based ferroelectric," J. Appl. Phys. 125(11), 114103 (2019).
- ³S. Y. Siew, B. Li, F. Gao, H. Y. Zheng, W. Zhang, P. Guo, S. W. Xie, A. Song, B. Dong, L. W. Luo, C. Li, X. Luo, and G.-Q. Lo, "Review of silicon photonics technology and platform development," J. Lightwave Technol. 39(13), 4374–4389 (2021).
- ⁴H. Lin, Z. Luo, T. Gu, L. C. Kimerling, K. Wada, A. Agarwal, and J. Hu, "Mid-infrared integrated photonics on silicon: A perspective," Nanophotonics 7(2), 393–420 (2017).
- ⁵A. E.-J. Lim, J. Song, Q. Fang, C. Li, X. Tu, N. Duan, K. K. Chen, R. P.-C. Tern, and T.-Y. Liow, "Review of silicon photonics foundry efforts," IEEE J. Sel. Top. Quantum Electron. **20**(4), 405–416 (2014).
- ⁶R. Krischek, W. Wieczorek, A. Ozawa, N. Kiesel, P. Michelberger, T. Udem, and H. Weinfurter, "Ultraviolet enhancement cavity for ultrafast nonlinear optics and high-rate multiphoton entanglement experiments," Nat. Photonics 4(3), 170–173 (2010)

- ⁷M. Karim, J. M. J. Lopes, and M. Ramsteiner, "The impact of ultraviolet laser excitation during Raman spectroscopy of hexagonal boron nitride thin films," J. Raman Spectrosc. 51(12), 2468–2477 (2020).
- ⁸N. Picqué and T. W. Hänsch, "Frequency comb spectroscopy," Nat. Photonics 13(3), 146–157 (2019).
- ⁹A. D. Ludlow, M. M. Boyd, J. Ye, E. Peik, and P. O. Schmidt, "Optical atomic clocks," Rev. Mod. Phys. 87(2), 637–701 (2015).
- ¹⁰A. Siddharth, T. Wunderer, G. Lihachev, A. S. Voloshin, C. Haller, R. N. Wang, M. Teepe, Z. Yang, J. Liu, J. Riemensberger, N. Grandjean, N. Johnson, and T. J. Kippenberg, "Near ultraviolet photonic integrated lasers based on silicon nitride," APL Photonics 7(4), 046108 (2022).
- ¹¹C. Xiong, W. H. P. Pernice, X. Sun, C. Schuck, K. Y. Fong, and H. X. Tang, "Aluminum nitride as a new material for chip-scale optomechanics and nonlinear optics," New J. Phys. 14(9), 095014 (2012).
 ¹²C. Xiong, W. H. P. Pernice, and H. X. Tang, "Low-loss, silicon integrated, alu-
- ¹²C. Xiong, W. H. P. Pernice, and H. X. Tang, "Low-loss, silicon integrated, aluminum nitride photonic circuits and their use for electro-optic signal processing," Nano Lett. 12(7), 3562–3568 (2012).
- ¹³C. Lin, J. S. D. Peñaranda, J. Dendooven, C. Detavernier, D. Schaubroeck, N. Boon, R. Baets, and N. Le Thomas, "UV photonic integrated circuits for far-field structured illumination autofluorescence microscopy," Nat. Commun. 13(1), 4360 (2022).
- ¹⁴C. Lin, D. Schaubroeck, R. Baets, N. Boon, and N. Le Thomas, "UV photonic-integrated-circuits-based structured illumination microscopy with a field of view larger than $100 \, \mu \text{m}^2$," IEEE J. Sel. Top. Quantum Electron. **29**(4), 1–9 (2023).
- 15G. Moody, V. J. Sorger, D. J. Blumenthal, P. W. Juodawlkis, W. Loh, C. Sorace-Agaskar, A. E. Jones, K. C. Balram, J. C. F. Matthews, A. Laing, M. Davanco, L. Chang, J. E. Bowers, N. Quack, C. Galland, I. Aharonovich, M. A. Wolff, C. Schuck, N. Sinclair, M. Lončar, T. Komljenovic, D. Weld, S. Mookherjea, S. Buckley, M. Radulaski, S. Reitzenstein, B. Pingault, B. Machielse, D. Mukhopadhyay, A. Akimov, A. Zheltikov, G. S. Agarwal, K. Srinivasan, J. Lu, H. X. Tang, W. Jiang, T. P. McKenna, A. H. Safavi-Naeini, S. Steinhauer, A. W. Elshaari, V. Zwiller, P. S. Davids, N. Martinez, M. Gehl, J. Chiaverini, K. K. Mehta, J. Romero, N. B. Lingaraju, A. M. Weiner, D. Peace, R. Cernansky, M. Lobino, E. Diamanti, L. T. Vidarte, and R. M. Camacho, "2022 roadmap on integrated quantum photonics," J. Phys. Photonics 4(1), 012501 (2022).
- 16_S. T. Jagsch, N. V. Triviño, F. Lohof, G. Callsen, S. Kalinowski, I. M. Rousseau, R. Barzel, J.-F. Carlin, F. Jahnke, R. Butté, C. Gies, A. Hoffmann, N. Grandjean, and S. Reitzenstein, "A quantum optical study of thresholdless lasing features in high-β nitride nanobeam cavities," Nat. Commun. 9(1), 564 (2018).
- ¹⁷A. W. Elshaari, W. Pernice, K. Srinivasan, O. Benson, and V. Zwiller, "Hybrid integrated quantum photonic circuits," Nat. Photonics 14(5), 285–298 (2020).
- ¹⁸F. W. Knollmann, A. N. Patel, and S. C. Doret, "Part-per-billion measurement of the $4^2S_{1/2} \rightarrow 3^2D_{5/2}$ electric-quadrupole-transition isotope shifts between ^{42,44,48}Ca⁺ and ⁴⁰Ca⁺," Phys. Rev. A **100**(2), 022514 (2019).
- ¹⁹C. Zhou, A. Ghods, V. G. Saravade, P. V. Patel, K. L. Yunghans, C. Ferguson, Y. Feng, B. Kucukgok, N. Lu, and I. T. Ferguson, "Review—The current and emerging applications of the III-nitrides," ECS J. Solid State Sci. Technol. 6(12), Q149 (2017).
- 20Y. Taniyasu, M. Kasu, and T. Makimoto, "An aluminium nitride light-emitting diode with a wavelength of 210 nanometres," Nature 441(7091), 325–328 (2006).
- ²¹T. Egawa, T. Jimbo, and M. Umeno, "Characteristics of InGaN/AlGaN light-emitting diodes on sapphire substrates," J. Appl. Phys. **82**(11), 5816–5821 (1997).
- ²²G. Kipshidze, V. Kuryatkov, B. Borisov, S. Nikishin, M. Holtz, S. n. g. Chu, and H. Temkin, "Deep ultraviolet AlGaInN-based light-emitting diodes on Si (111) and sapphire," Phys. Status Solidi A 192(2), 286–291 (2002).
- ²³J. Zhang, X. Hu, A. Lunev, J. Deng, Y. Bilenko, T. M. Katona, M. S. Shur, R. Gaska, and M. A. Khan, "AlGaN deep-ultraviolet light-emitting diodes," Jpn. J. Appl. Phys. 44(10R), 7250 (2005).
- ²⁴M. A. Khan, M. Shatalov, H. P. Maruska, H. M. Wang, and E. Kuokstis, "III–nitride UV devices," Jpn. J. Appl. Phys. 44(10R), 7191 (2005).

- 25T. Wunderer, C. L. Chua, J. E. Northrup, Z. Yang, N. M. Johnson, M. Kneissl, G. A. Garrett, H. Shen, M. Wraback, B. Moody, H. S. Craft, R. Schlesser, R. F. Dalmau, and Z. Sitar, "Optically pumped UV lasers grown on bulk AlN substrates," Phys. Status Solidi C 9(3–4), 822–825 (2012).
- ²⁶N. Alfaraj, J.-W. Min, C. H. Kang, A. A. Alatawi, D. Priante, R. C. Subedi, M. Tangi, T. K. Ng, and B. S. Ooi, "Deep-ultraviolet integrated photonic and optoelectronic devices: A prospect of the hybridization of group III-nitrides, III-oxides, and two-dimensional materials," J. Semicond. 40(12), 121801 (2019).
- ²⁷B. K. SaifAddin, A. S. Almogbel, C. J. Zollner, F. Wu, B. Bonef, M. Iza, S. Nakamura, S. P. DenBaars, and J. S. Speck, "AlGaN deep-ultraviolet light-emitting diodes grown on SiC substrates," ACS Photonics 7(3), 554–561 (2020).

 ²⁸M. Kneissl, T. Kolbe, C. Chua, V. Kueller, N. Lobo, J. Stellmach, A. Knauer, H. Bedginger, S. Fijfeldt, Z. Yang, N. M. Johnson, and M. Weyere, "Advances in
- H. Rodriguez, S. Einfeldt, Z. Yang, N. M. Johnson, and M. Weyers, "Advances in group III-nitride-based deep UV light-emitting diode technology," Semicond. Sci. Technol. **26**(1), 014036 (2011).
- ²⁹M. Shatalov, W. Sun, Y. Bilenko, A. Sattu, X. Hu, J. Deng, J. Yang, M. Shur, C. Moe, M. Wraback, and R. Gaska, "Large chip high power deep ultraviolet light-emitting diodes," Appl. Phys. Express 3(6), 062101 (2010).
- ³⁰B. So, J. Kim, T. Kwak, T. Kim, J. Lee, U. Choi, and O. Nam, "Improved carrier injection of AlGaN-based deep ultraviolet light emitting diodes with graded superlattice electron blocking layers," RSC Adv. 8(62), 35528–35533 (2018).
- ³¹C. Manz, S. Leone, L. Kirste, J. Ligl, K. Frei, T. Fuchs, M. Prescher, P. Waltereit, M. A. Verheijen, A. Graff, M. Simon-Najasek, F. Altmann, M. Fiederle, and O. Ambacher, "Improved AlScN/GaN heterostructures grown by metal-organic chemical vapor deposition," Semicond. Sci. Technol. 36(3), 034003 (2021).
- ³²R. K. Mondal, S. Adhikari, V. Chatterjee, and S. Pal, "Recent advances and challenges in AlGaN-based ultra-violet light emitting diode technologies," <u>Mater. Res. Bull.</u> 140, 111258 (2021).
- ³³K. X. Chen, Q. Dai, W. Lee, J. K. Kim, E. F. Schubert, J. Grandusky, M. Mendrick, X. Li, and J. A. Smart, "Effect of dislocations on electrical and optical properties of n-type Al_{0.34}Ga_{0.66}N," Appl. Phys. Lett. **93**(19), 192108 (2008).

 ³⁴H. Hirayama, T. Yatabe, N. Noguchi, and N. Kamata, "Development of a
- 3⁴H. Hirayama, T. Yatabe, N. Noguchi, and N. Kamata, "Development of § 230–270 nm AlGaN-based deep-UV LEDs," Electron. Commun. Jpn. **93**(3), § 24–33 (2010).
- 55 D. Doppalapudi and T. D. Moustakas, in *Handbook of Thin Films*, edited by B. H. Singh Nalwa (Academic Press, Burlington, 2002), pp. 57–115.
- ³⁶E. A. Boardman, L. S.-W. Huang, J. J. Robson-Hemmings, T. M. Smeeton, S. E. Hooper, and J. Heffernan, "Deep ultraviolet (UVC) laser for sterilisation and fluorescence applications," Sharp Tech. Rept. 104, 31–35 (2012).
- 37T. Wang, B. Liu, Y. Lin, Q. Yang, W. Gao, M. J. Li, J. Qiu, X. Yu, X. Xu, and S. F. Yu, "Ultraviolet C lasing at 263 nm from Ba₂LaF₇:Yb³⁺, Tm³⁺ upconversion nanocrystal microcavities," Opt. Lett. 45(21), 5986–5989 (2020).
- ³⁸C. Xiong, W. Pernice, C. Schuck, and H. X. Tang, "Second harmonic generation in aluminum nitride waveguides on silicon substrates," in *Conference on Lasers and Electro-Optics* (Optical Society of America, 2012), p. QF3G.4.
- ³⁹X. Guo, C.-L. Zou, and H. X. Tang, "Second-harmonic generation in aluminum nitride microrings with 2500%/W conversion efficiency," Optica 3(10), 1126–1131 (2016).
- ⁴⁰T. Troha, M. Rigler, D. Alden, I. Bryan, W. Guo, R. Kirste, S. Mita, M. D. Gerhold, R. Collazo, Z. Sitar, and M. Zgonik, "UV second harmonic generation in AlN waveguides with modal phase matching," Opt. Mater. Express 6(6), 2014–2023 (2016).
- ⁴¹V. Yoshioka, J. Lu, Z. Tang, J. Jin, R. H. Olsson III, and B. Zhen, "Strongly enhanced second-order optical nonlinearity in CMOS-compatible $Al_{1-x}Sc_xN$ thin films," APL Mater. **9**(10), 101104 (2021).
- ⁴²D. Zhu, L. Shao, M. Yu, R. Cheng, B. Desiatov, C. J. Xin, Y. Hu, J. Holzgrafe, S. Ghosh, A. Shams-Ansari, E. Puma, N. Sinclair, C. Reimer, M. Zhang, and M. Lončar, "Integrated photonics on thin-film lithium niobate," Adv. Opt. Photonics 13(2), 242 (2021).
- ⁴³Y. Qi and Y. Li, "Integrated lithium niobate photonics," Nanophotonics 9(6), 1287–1320 (2020).

- ⁴⁴R. W. Boyd, in *Nonlinear Optics*, 4th ed., edited by R. W. Boyd (Academic Press, 2020), pp. 65–135.
- ⁴⁵A. Majkić, U. Puc, A. Franke, R. Kirste, R. Collazo, Z. Sitar, and M. Zgonik, "Optical properties of aluminum nitride single crystals in the THz region," Opt. Mater. Express 5(10), 2106–2111 (2015).
- ⁴⁶D. S. Hum and M. M. Fejer, "Quasi-phasematching," C. R. Phys. 8(2), 180–198 (2007).
- A7S. Zhu, Q. Zhong, T. Hu, et al., "Aluminum nitride ultralow loss waveguides and push-pull electro-optic modulators for near infrared and visible integrated photonics," in *Optical Fiber Communication Conference (OFC)* 2019, OSA Technical Digest, San Diego, CA (Optical Society of America, 2019), p. W2A.11.
 A8A. Soltani, A. Stolz, J. Charrier, M. Mattalah, J.-C. Gerbedoen, H. A. Barkad, V. Mortet, M. Rousseau, N. E. Bourzgui, A. Benmoussa, and J.-C. De Jaeger, "Dispersion properties and low infrared optical losses in epitaxial AlN on sapphire substrate in the visible and infrared range," J. Appl. Phys. 115(16), 163515 (2014).
- 49 M. Baeumler, Y. Lu, N. Kurz, L. Kirste, M. Prescher, T. Christoph, J. Wagner, A. Žukauskaitė, and O. Ambacher, "Optical constants and band gap of wurtzite $Al_{1-x}Sc_xN/Al_2O_3$ prepared by magnetron sputter epitaxy for scandium concentrations up to x=0.41," J. Appl. Phys. 126(4), 045715 (2019).
- 50 R. Deng, S. R. Evans, and D. Gall, "Bandgap in $Al_{1-x}Sc_xN$," Appl. Phys. Lett. **102**(11), 112103 (2013).
- ⁵¹S. Zhang, D. Holec, W. Y. Fu, C. J. Humphreys, and M. A. Moram, "Tunable optoelectronic and ferroelectric properties in Sc-based III-nitrides," J. Appl. Phys. 114(13), 133510 (2013).
- 52Y.-F. Chen, S.-N. Zhu, Y.-Y. Zhu, N.-B. Ming, B.-B. Jin, and R.-X. Wu, "High-frequency resonance in acoustic superlattice of periodically poled LiTaO₃," Appl. Phys. Lett. **70**(5), 592–594 (1997).
- ⁵³I. V. Ostrovskii and A. B. Nadtochiy, "Domain resonance in two-dimensional periodically poled ferroelectric resonator," Appl. Phys. Lett. 86(22), 222902 (2005).
- ⁵⁴I. V. Ostrovskii and A. B. Nadtochiy, "Free vibration of periodically poled ferroelectric plate," J. Appl. Phys. 99(11), 114106 (2006).
- E. Courjon, N. Courjal, W. Daniau, G. Lengaigne, L. Gauthier-Manuel,
 S. Ballandras, and J. Hauden, "Lamb wave transducers built on periodically poled Z-cut LiNbO₃ wafers," J. Appl. Phys. 102(11), 114107 (2007).
 E. Courjon, F. Bassignot, G. Ulliac, S. Benchabane, and S. Ballandras,
- ⁵⁶E. Courjon, F. Bassignot, G. Ulliac, S. Benchabane, and S. Ballandras, "Acoustic wave filter based on periodically poled lithium niobate," IEEE Trans Ultrason Ferroelectr Freq Control 59(9), 1942–1949 (2012).
- ⁵⁷S. Rassay, D. Mo, C. Li, N. Choudhary, C. Forgey, and R. Tabrizian, "Intrinsically switchable ferroelectric scandium aluminum nitride lamb-mode resonators," IEEE Electron Device Lett. 42(7), 1065–1068 (2021).
- 58S. Rassay, D. Mo, and R. Tabrizian, "Dual-mode scandium-aluminum nitride lamb-wave resonators using reconfigurable periodic poling," Micromachines 13(7), 1003 (2022).
- ⁵⁹D. Feng, N. Ming, J. Hong, Y. Yang, J. Zhu, Z. Yang, and Y. Wang, "Enhancement of second-harmonic generation in LiNbO₃ crystals with periodic laminar ferroelectric domains," Appl. Phys. Lett. **37**, 607–609 (1980).
- ⁶⁰J. A. Armstrong, N. Bloembergen, J. Ducuing, and P. S. Pershan, "Interactions between light waves in a nonlinear dielectric," Phys. Rev. 127(6), 1918–1939 (1962).
- ⁶¹P. A. Franken and J. F. Ward, "Optical harmonics and nonlinear phenomena," Rev. Mod. Phys. 35(1), 23–39 (1963).
- ⁶²S. Pezzagna, P. Vennéguès, N. Grandjean, A. D. Wieck, and J. Massies, "Submicron periodic poling and chemical patterning of GaN," Appl. Phys. Lett. 87(6), 062106 (2005).
- ⁶³M. Stutzmann, O. Ambacher, M. Eickhoff, U. Karrer, A. Lima Pimenta, R. Neuberger, J. Schalwig, R. Dimitrov, P. j. Schuck, and R. d. Grober, "Playing with polarity," Phys. Status Solidi B 228(2), 505–512 (2001).
- 64A. Chowdhury, H. M. Ng, M. Bhardwaj, and N. G. Weimann, "Second-harmonic generation in periodically poled GaN," Appl. Phys. Lett. 83(6), 1077–1079 (2003).

- ⁶⁵J. Hite, M. Twigg, M. Mastro, J. Freitas, J. Meyer, I. Vurgaftman, S. O'Connor, N. Condon, F. Kub, S. Bowman, and C. Eddy, "Development of periodically oriented gallium nitride for non-linear optics [invited]," Opt. Mater. Express 2(9), 1203–1208 (2012).
- ⁶⁶J. K. Hite, N. Y. Garces, R. Goswami, M. A. Mastro, F. J. Kub, and C. R. Eddy, "Selective switching of GaN polarity on Ga-polar GaN using atomic layer deposited Al₂O₃," Appl. Phys. Express 7(2), 025502 (2014).
- ⁶⁷S. R. Bowman, C. G. Brown, J. K. Hite, J. A. Freitas, F. J. Kub, C. R. Eddy, I. Vurgaftman, J. R. Meyer, J. H. Leach, and K. Udwary, "Harmonic Generation in Periodically Oriented Gallium Nitride," in *Lasers Congress 2016 (ASSL, LSC, LAC)*, OSA Technical Digest (online) (Optica Publishing Group, 2016), p. ATu5A.3.
- p. ATu5A.3.

 68 D. Alden, W. Guo, R. Kirste, F. Kaess, I. Bryan, T. Troha, A. Bagal, P. Reddy, L. H. Hernandez-Balderrama, A. Franke, S. Mita, C.-H. Chang, A. Hoffmann, M. Zgonik, R. Collazo, and Z. Sitar, "Fabrication and structural properties of AlN submicron periodic lateral polar structures and waveguides for UV-C applications," Appl. Phys. Lett. 108(26), 261106 (2016).
- ⁶⁹D. Alden, T. Troha, R. Kirste, S. Mita, Q. Guo, A. Hoffmann, M. Zgonik, R. Collazo, and Z. Sitar, "Quasi-phase-matched second harmonic generation of UV light using AlN waveguides," Appl. Phys. Lett. 114(10), 103504 (2019).
- 70Y. Glickman, E. Winebrand, A. Arie, and G. Rosenman, "Electron-beam-induced domain poling in LiNbO₃ for two-dimensional nonlinear frequency conversion," Appl. Phys. Lett. 88(1), 011103 (2006).
- 71_{L. M.} Mazur, S. Liu, X. Chen, W. Krolikowski, and Y. Sheng, "Localized ferroelectric domains via laser poling in monodomain calcium barium niobate crystal," Laser Photonics Rev. **15**(9), 2100088 (2021).
- 72I. Krasnokutska, J.-L. J. Tambasco, and A. Peruzzo, "Submicron domain engineering in periodically poled lithium niobate on insulator" arXiv:2108.10839 (2021).
 73A. Suceava, J. Hayden, K. Kelley, Y. Xiong, B. Fazlioglu-Yalcin, I. Dabo, S. Trolier-McKinstry, J.-P. Maria, and V. Gopalan, "Enhancement of second-order optical nonlinearities and nanoscale periodic domain patterning in ferroelectric boron-substituted aluminum nitride thin films," Opt. Mater. Express 13, 9
- 74V. Y. Shur, R. G. Batchko, E. L. Rumyantsev, G. D. Miller, M. M. Fejer, and R. L. Byer, in *ISAF 1998. Proceedings of the Eleventh IEEE International Symposium on Applications of Ferroelectrics (Cat. No. 98CH36245)* (IEEE, 1998), pp. 399–405.
- 75M. Yamada, N. Nada, M. Saitoh, and K. Watanabe, "First-order quasi-phase matched LiNbO₃ waveguide periodically poled by applying an external field for efficient blue second-harmonic generation," Appl. Phys. Lett. **62**(5), 435–436 (1993).
- ⁷⁶J. Brockmeier, P. W. M. Mackwitz, M. Rüsing, C. Eigner, L. Padberg, M. Santandrea, C. Silberhorn, A. Zrenner, and G. Berth, "Non-invasive visualization of ferroelectric domain structures on the non-polar y-surface of KTiOPO₄ via Raman imaging," Crystals 11(9), 1086 (2021).
- via Raman imaging," Crystals 11(9), 1086 (2021).

 77
 J. Nordlander, F. Eltes, M. Reynaud, J. Nürnberg, G. De Luca, D. Caimi, A. A. Demkov, S. Abel, M. Fiebig, J. Fompeyrine, and M. Trassin, "Ferroelectric domain architecture and poling of BaTiO₃ on Si," Phys. Rev. Mater. 4(3), 034406 (2020).
- ⁷⁸G. Esteves, M. Berg, K. D. Wrasman, M. David Henry, B. A. Griffin, and E. A. Douglas, "CMOS compatible metal stacks for suppression of secondary grains in Sc_{0.125}Al_{0.875}N," J. Vac. Sci. Technol. A 37(2), 021511 (2019).
- 79Y. Liu, T. Kamei, K. Endo, S. O'uchi, J. Tsukada, H. Yamauchi, T. Hayashida, Y. Ishikawa, T. Matsukawa, K. Sakamoto, A. Ogura, and M. Masahara, "Nanoscale wet etching of physical-vapor-deposited titanium nitride and its application to sub-30-nm-gate-length fin-type double-gate metal-oxide-semi-conductor field-effect transistor fabrication," Jpn. J. Appl. Phys. 49(6S), 06GH18 (2010).
- 80Z. Tang, G. Esteves, J. Zheng, and R. H. Olsson, "Vertical and lateral etch survey of ferroelectric AlN/Al_{1-x}Sc_xN in aqueous KOH solutions," Micromachines 13(7), 1066 (2022).
- ⁸¹C. s. Sandu, F. Parsapour, S. Mertin, V. Pashchenko, R. Matloub, T. LaGrange, B. Heinz, and P. Muralt, "Abnormal grain growth in AlScN thin films induced by complexion formation at crystallite interfaces," Phys. Status Solidi A 216, 1800569 (2019).

- 82D. Wang, J. Zheng, P. Musavigharavi, W. Zhu, A. C. Foucher, S. E. Trolier-McKinstry, E. A. Stach, and R. H. Olsson, "Ferroelectric switching in sub-20 nm aluminum scandium nitride thin films," IEEE Electron Device Lett. 41(12), 1774–1777 (2020).
- 83S. Fichtner, F. Lofink, B. Wagner, G. Schönweger, T.-N. Kreutzer, A. Petraru, and H. Kohlstedt, in 2020 Joint Conference of the IEEE International Frequency Control Symposium and International Symposium on Applications of Ferroelectrics (IFCS-ISAF) (IEEE, 2020), pp. 1–4.
- ⁸⁴D. Wang, P. Musavigharavi, J. Zheng, G. Esteves, X. Liu, M. M. A. Fiagbenu, E. A. Stach, D. Jariwala, and R. H. Olsson III, "Sub-microsecond polarization switching in (Al,Sc)N ferroelectric capacitors grown on complementary metal-oxide-semiconductor-compatible aluminum electrodes," Phys. Status Solidi RRL 15(5), 2000575 (2021).
- ⁸⁵W. Zhu, J. Hayden, F. He, J.-I. Yang, P. Tipsawat, M. D. Hossain, J.-P. Maria, and S. Trolier-McKinstry, "Strongly temperature dependent ferroelectric switching in AlN, $Al_{1-x}Sc_xN$, and $Al_{1-x}B_xN$ thin films," Appl. Phys. Lett. **119**(6), 062901 (2021).
- ⁸⁶D. Drury, K. Yazawa, A. Zakutayev, B. Hanrahan, and G. Brennecka, "High-temperature ferroelectric behavior of Al_{0.7}Sc_{0.3}N," Micromachines 13(6), 887 (2022).
- ⁸⁷W. Guo, R. Kirste, I. Bryan, Z. Bryan, L. Hussey, P. Reddy, J. Tweedie, R. Collazo, and Z. Sitar, "KOH based selective wet chemical etching of AlN, Al_xGa_{1-x}N, and GaN crystals: A way towards substrate removal in deep ultraviolet-light emitting diode," Appl. Phys. Lett. 106(8), 082110 (2015).
- 88 N. Wolff, S. Fichtner, B. Haas, M. R. Islam, F. Niekiel, M. Kessel, O. Ambacher, C. Koch, B. Wagner, F. Lofink, and L. Kienle, "Atomic scale

- confirmation of ferroelectric polarization inversion in wurtzite-type AlScN," J. Appl. Phys. 129(3), 034103 (2021).
- ⁸⁹V. Y. Shur, "Kinetics of ferroelectric domains: Application of general approach to LiNbO₃ and LiTaO₃," J. Mater. Sci. **41**(1), 199–210 (2006).
- ⁹⁰V. Y. Shur and A. R. Akhmatkhanov, "Domain shape instabilities and dendrite domain growth in uniaxial ferroelectrics," Philos. Trans. R. Soc. A **376**(2113), 20170204 (2018).
- ⁹¹V. Y. Shur, E. V. Pelegova, A. P. Turygin, M. S. Kosobokov, and Y. M. Alikin, "Forward growth of ferroelectric domains with charged domain walls. Local switching on non-polar cuts," J. Appl. Phys. 129(4), 044103 (2021).
- ⁹² A. L. Kholkin, S. V. Kalinin, A. Roelofs, and A. Gruverman, in *Scanning Probe Microscopy*, edited by S. Kalinin and A. Gruverman (Springer, New York, 2007), pp. 173–214.
- pp. 173-214.

 ⁹³A. Gruverman, M. Alexe, and D. Meier, "Piezoresponse force microscopy and nanoferroic phenomena," Nat. Commun. **10**(1), 1661 (2019).
- 94O. Kwon, D. Seol, H. Qiao, and Y. Kim, "Recent progress in the nanoscale evaluation of piezoelectric and ferroelectric properties via scanning probe microscopy," Adv. Sci. 7(17), 1901391 (2020).
- 95Y. J. Kim, H. W. Park, S. D. Hyun, H. J. Kim, K. D. Kim, Y. H. Lee, T. Moon, Y. B. Lee, M. H. Park, and C. S. Hwang, "Voltage drop in a ferroelectric single layer capacitor by retarded domain nucleation," Nano Lett. 17(12), 7796–7802 (2017).
- 96. M. Yang and Y. Kim, "Nanoscale probing of ferroelectric domain switching using piezoresponse force microscopy," J. Korean Ceram. Soc. 56(4), 340–349 (2019).
- piezoresponse force microscopy," J. Korean Ceram. Soc. **56**(4), 340–349 (2019). **97**M. M. Fejer, G. A. Magel, D. H. Jundt, and R. L. Byer, "Quasi-phase-matched second harmonic generation: Tuning and tolerances," IEEE J. Quantum Electron. **28**(11), 2631–2654 (1992).